Design and synthesis of benzothiadiazole-based molecular systems: self-assembly, optical and electronic properties

Montserrat Miranda-Olvera, Rafael Arcos-Ramos, Mauricio Maldonado-Domínguez, Lionel Salmon, Gábor Molnár, Azzedine Bousseksou, María del Pilar Carreón-Castro

ARTICLE

Design and synthesis of benzothiadiazole-based molecular systems: self-assembly, optical and electronic properties

Received 00th January 20xx,
Accepted 00th January 20xx

DOI: 10.1039/x0xx00000x

Montserrat Miranda-Olvera,[a,b] Rafael Arcos-Ramos,[a] Mauricio Maldonado-Domínguez,[c] Lionel Salmon,[b] Gábor Molnár,[b] Azzedine Bousseksou,[b] and María del Pilar Carreón-Castro[a*]

A set of small benzothiadiazole (BTD)-based derivatives with a D-A-D architecture was synthesized and characterized as building blocks of organic semiconducting materials by applying an experimental-theoretical approach. The four derivatives tend to self-assemble into highly ordered crystalline solids which, with varying degrees of responsiveness to mechanical and thermal stimuli. The featured derivatives exhibit absorption maxima in solution and molar extinction coefficient values related to π-π* electronic transitions with minor solvatochromic response, displaying broad fluorescence profiles with large Stokes shifts and high quantum fluorescence yields. In the solid-state, the BTD derivatives display absorption maxima in the visible range between and intense fluorescence emission for the n-butoxy and fluorene derivatives. The stability of the one-electron reduced and oxidized forms of all compounds was assessed by means of cyclic voltammetry which, complemented by DFT calculations allowed identifying one BTD derivative (BuO-BTD) as a strong candidate for use as electron transport layer in organoelectronic devices.

Introduction

Multifunctional materials for organic electronics can be readily accessed through the engineering of small supramolecular building-blocks capable to modulate their self-assembly into highly ordered arrangements in the solid-state. In this sense, π-conjugated organic systems have attracted considerable interest during the past decades due to their wide structural versatility and remarkable optical and electronic properties.[1-5] Principally, π-conjugated small-organic molecules are evolving active-layer components for applications in organic photovoltaics reaching equivalent photo-conversion efficiencies to that of polymers.[6-8]

A useful strategy to improve charge transport through π-conjugated frameworks is based on designing molecular structures with electron-donor and electron-withdrawing moieties on a discrete entity. In general, for donor-acceptor (D-A) architectures, the HOMO (Highest Occupied Molecular Orbital) and LUMO (Lowest Unoccupied Molecular Orbital) band gap can be tuned to enhance holes and electrons transport through the π-conjugated system, due to the efficient charge transfer processes from the ground excited state and light absorption increase.[9-13] Despite of numerous advances in organic semiconducting materials development; solution-processable compounds with chemical stability and high performance are still required. Among the representative electron-accepting small-organic molecules used in this field, benzothiadiazole (BTD) based conjugated molecules display remarkable electric and optical responsivity,[14-18] coupled to a fair chemical stability and high electron affinity.[14,19] In this context, the BTD-fragment has been used as a molecular design motif in the development of molecular and polymeric materials for organic electronic applications. Due to the electron-withdrawing nature of the BTD core, it can be exploited as a building block for n-type semiconductors. The symmetrical functionalization with aryl- or heteroaryl-moieties facilitates intramolecular charge transfer (ICT) processes which allow the fine-tuning of their optical and electronic properties.[20-23] In addition, 4,7-diaryl-benzothiadiazole derivatives substituted with flexible alkoxy chains display interesting liquid crystal properties. Several BTD-based smectic and nematic liquid crystals have been used as highly dichroic fluorescent dyes for liquid crystal displays and as active layers in organic field effect transistors (OFETs).[20,24-26]

Small π-conjugated structures based on benzothiadiazole (BTD) derivatives can afford self-assembled supramolecular arrangements.[27-29] In particular, rod-shaped donor-acceptor-donor (D-A-D) architectures where BTD acts as a central electron-withdrawing (A) core, attached to alkyl/alkoxy (R, OR) electron-donor (D) units, have been extensively used as liquid crystals.[30-32]

[a] Departamento de Química de Radiaciones y Radioquímica, Instituto de Ciencias Nucleares, Universidad Nacional Autónoma de México, 04510, Ciudad de México, México. e-mail: pilar@nucleares.unam.mx
[b] Laboratoire de Chimie de Coordination, CNRS UPR 8241, 205 route de Narbonne, Toulouse, F-31077 France
[c] J. Heyrovský Institute of Physical Chemistry, Czech Academy of Science, Dolejškova 2155/3, 182 23 Prague 8, Czech Republic.
† Footnotes relating to the title and/or authors should appear here.
Electronic Supplementary Information (ESI) available: CCDC **2128949** (BuO-BTD). For ESI and crystallographic data in CIF or other electronic format see DOI: 10.1039/x0xx00000x

The (alkoxy-substituted-phenyl)-benzothiadiazole derivatives are well-known fluorescent dyes with π-conjugated rod-shaped structures that display liquid crystal properties.[24] These types of fluorescent dyes have been emerged as promising supramolecular building blocks of homogeneous thin-films with reduced defects and with multi-layered π-stacked arrangements useful for charge transport processes.[33-34] Charge transport in semiconductor organic solids is facilitated when periodic π-stacking interactions are present, and evidence suggests that it is most favored when the stacking vector is aligned with that of the charge transport;[35-36] noteworthy, this kind of supramolecular organization is often present in a wide variety of BTD-based derivatives.

In general, the structural variation of the electron-donor substituents modifies the capacity of these molecules to self-assemble in single-crystals or liquid crystals and allows thus to fine-tune their optical and electronic properties. In the present work, we selected the 4,7-diphenyl-substituted-benzothiadiazole as basic core, due to its remarkable luminescent response in solution and we explored the effect of the different supramolecular arrangements on the optical and electronic properties of 4,7-bis(alkoxy-substituted-phenyl)- and 4,7-bis(dibenzofuran(DBF)/fluorene(FL)-substituted)-benzothiadiazoles.

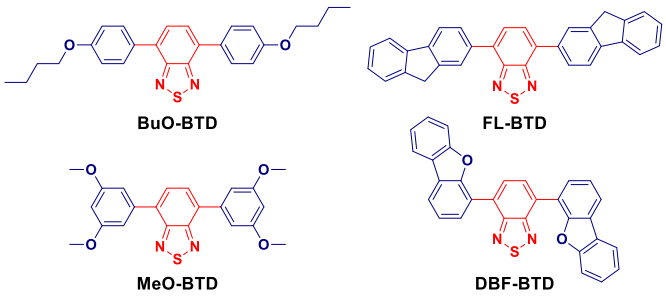

Scheme 1. Benzothiadiazole-based D-A-D derivatives.

Results and Discussion

Synthesis

We synthesized four BTD-derivatives (with methoxy, butoxy, fluorene and dibenzofurane substituents) using Pd-catalyzed Suzuki coupling reaction in moderate to good yields (Scheme 1). Each compound was purified by successive recrystallization with $CHCl_3$/toluene mixture and characterized by liquid NMR (^1H, ^{13}C), FTIR and HRMS (*see* ESI).

Solid-state characterization. Thermal analysis and X-Ray diffraction experiments

Freshly recrystallized samples (from chloroform) of BTD derivatives were studied by differential scanning calorimetry (DSC) and thermogravimetric analysis (TGA) to ascertain their thermal stability upon heating in the range 25−800 °C (*see* ESI). In all DSC experiments, a sharp endothermic transition that corresponds with the visual observation of the melting point was found; no additional transitions due to solvent loss or phase change were found in the 20-100°C range.

In order to explore the influence of the donor groups on the solid-state organization of the BTD derivatives, we attempted to grow single crystals of the different compounds with chloroform, toluene and chloroform/toluene mixture. For **BuO-BTD**, high-quality single-crystals suitable for X-ray diffraction analysis have been obtained after slow evaporation of a toluene solution in a partially open glass vial. **BuO-BTD** crystallizes in the orthorhombic space group Pnca with Z = 12 and two independent units per asymmetric unit (*see* ESI for crystal data). The two molecules are antiparallelly aligned and display slightly different torsion angles between the butoxy-substituted-phenyl and the BTD core (35.17/35.82° and 36.88°). In one of the molecules, the alcoxy-substituted-phenyl are involved in intermolecular interactions (C-H···N, 2.66 Å) with the benzothiadiazole core producing a one-dimensional *zig-zag* arrangement, locating the BTD rings in a parallel displaced manner (Figure 1a). In the other molecule, C-H···π (*ca.* 2.82 Å) interactions between neighboring phenyl rings produce a π-stacked columnar arrangement locating the BTD rings in an antiparallel mode with interplanar distances (*centroid-centroid*) of *ca*. 3.8 Å (Figure 1b). These one-dimensional arrangements are self-assembled through the butyl-chains (interidigation) in a highly dense supramolecular structure that contains different intermolecular contacts between planar π-units (Figure 1c).

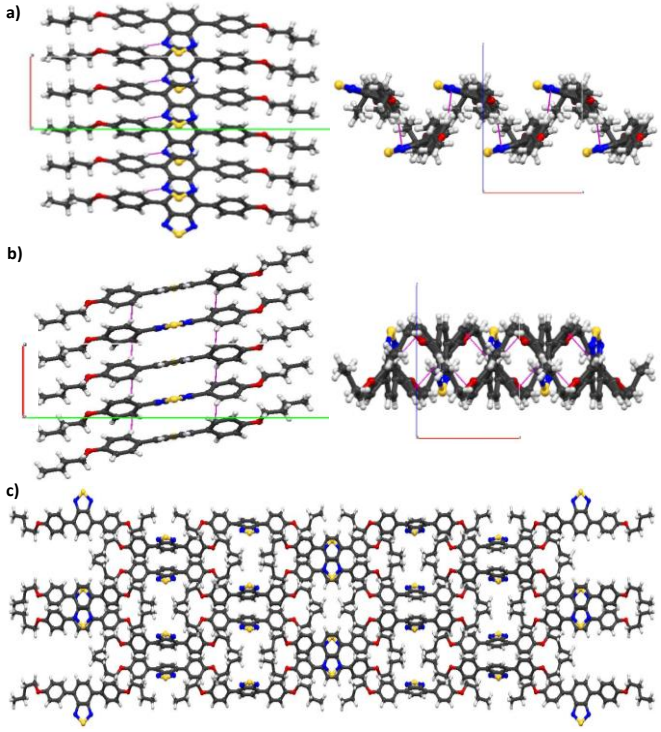

Figure 1. (a, b) Intermolecular interactions and (c) crystal packing of **BuO-BTD**.

Subsequently, we further explored how the different electron-donor groups modify the capacity of these molecules to self-

assembly in the solid-state by means of powder X-Ray diffraction (PXRD) on recrystallized (from chloroform), ground (mechanical stimulus) and annealed at 100°C (thermal stimulus) samples. The XRD patterns of the powders displayed sharp Bragg diffraction peaks in the 5-60 degrees (2θ) range indicating crystallinity of the samples (Figure 2).

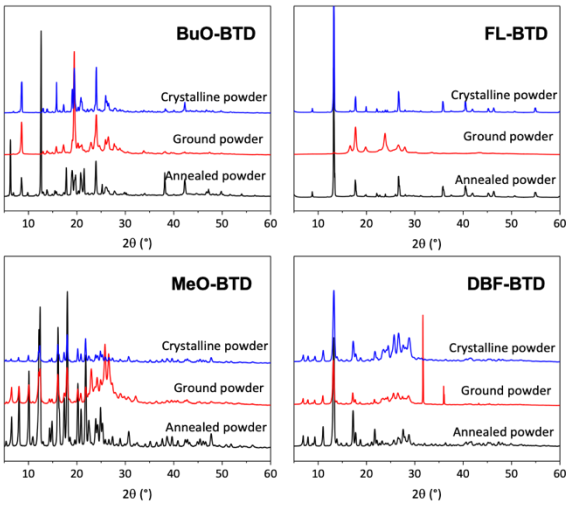

Figure 2. PXRD diffractograms of BTD derivatives of crystallized, ground and annealed (at 100°C) powders.

Powder X-Ray diffractograms of the butoxy-derivative displayed intense and sharp peaks between 10 to 50 degrees, which only vary in intensity upon mechanical or thermal stimuli. For fluorene derivative, the diffractogram of the crystalline powder displays two important peaks at 13.2° and 26.1° with corresponding spacing's of 6.7 and 3.4 Å, respectively. The theta value can be assigned to *face-to-face* distances between adjacent π-conjugated entities in 1D-supramolecular arrangements. Grinding this crystalline sample significantly affects the diffraction pattern with the appearance of peaks at 17.7 and 23.9° and the disappearance of the previous peaks. On the other hand, the thermal treatment (at 100 °C) does not produce a significant change. In the case of dibenzofuran-derivative, the diffractogram of the crystalline powder display well-resolved peak including two main peaks at 13.2° and 17.2° (corresponding to spacings of 6.7 and 5.2 Å). The mechanical treatment considerably modifies the powder pattern, reducing the intensity of the main peak at 13.2°, and inducing the appearance of peaks at 31.6 and 35.9° (2.8 and 2.5 Å, respectively); while thermal treatment slightly affects the diffraction peaks up to 20°. Finally, dimethoxy-derivative diffractograms of crystalline, ground, and annealed samples present larger number of well-resolved peaks, suggesting a more complex degree of structural order or a coexistence of crystalline phases. In particular, the thermal treatment elicits an improvement change of the crystallinity as indicated by the appearance of diffraction peaks between 30° and 50°.

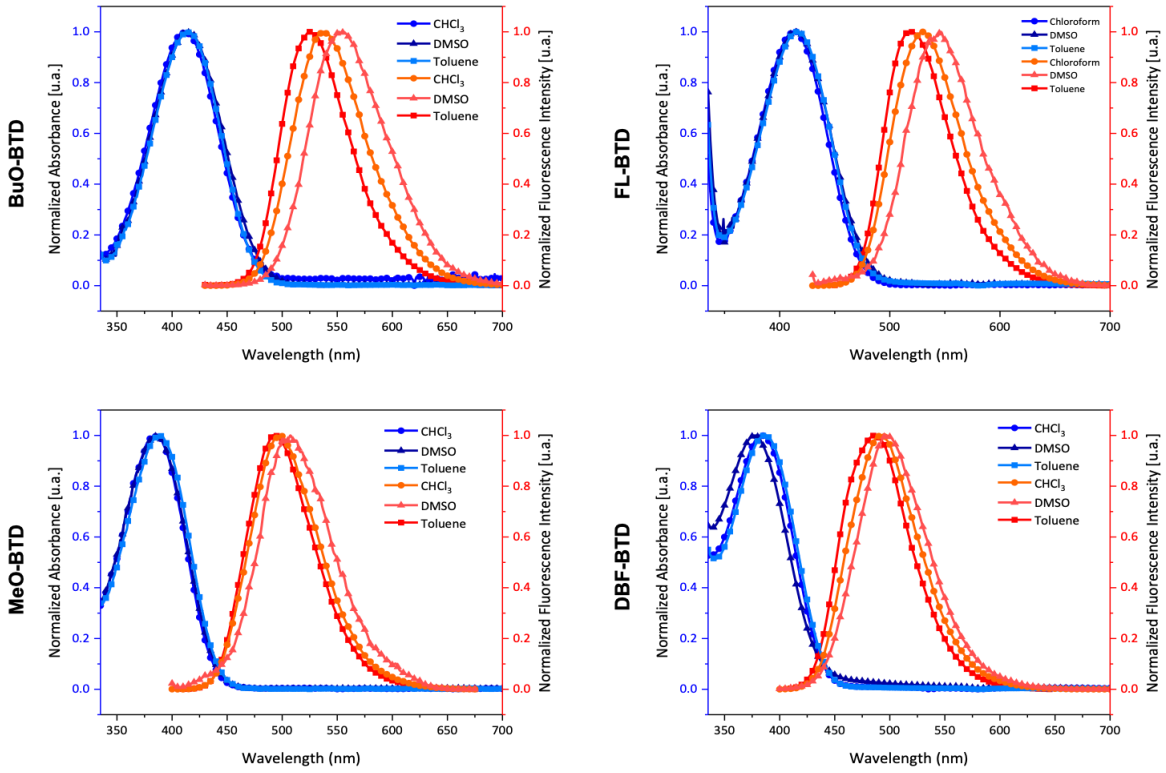

Figure 3. UV-Vis and fluorescence profiles of BTD-based building blocks in different solvents.

Solvent	BuO-BTD				FL-BTD				MeO-BTD				DBF-BTD			
	Toluene	$CHCl_3$	DMSO	Solid-state	Toluene	$CHCl_3$	DMSO	Solid-state	Toluene	$CHCl_3$	DMSO	Solid-state	Toluene	$CHCl_3$	DMSO	Solid-state
λ_{abs} (nm)	413	412	415	478	416	413	415	469	388	384	385	455	387	382	375	448
λ_{em} (nm)	527	534	551	546	518	532	545	540	495	498	508	516	486	491	498	532
Stokes shift ν (cm^{-1})	5237	5545	5948	2605	4733	5125	5748	2803	5571	5961	6289	2564	5264	5811	6586	3224
Φ_f	0.57	0.43	0.36	--	0.60	0.55	0.27	--	0.77	0.71	0.05	--	0.91	0.78	0.60	--

Table 1. Relevant absorption and fluorescence emission data of BTD-based building blocks in solid state and in different solvents.

Optical properties

Initially, we investigated how the different electronic nature of the electron donor groups attached to the benzothiadiazole core influence the optical properties of the BTD-based derivatives by means of optical spectroscopy (UV-Vis absorption and fluorescence) (Figure 3). The relevant data are summarized in table 1. Absorption profiles of BTD-based derivatives were determined in different organic solvents at room temperature (Table S2). The four derivatives display absorption bands assigned to π-π* transitions of the BTD core and to charge transfer (CT) transitions. In general, absorption maxima (λ_{max}) of compounds were located between 405-416 nm (**FL-BTD**), 373-387 nm (**DBF-BTD**), 381-388 nm (**MeO-BTD**), and 406-415 nm (**BuO-BTD**). The changes in the solvent polarity afforded slight solvatochromic shifts with no clear dependence on the environment polarity suggesting that the transition dipole moment is only weakly affected by the differential functionalization.

In addition, all derivatives exhibit intense fluorescence in solution with emission maxima (λ_{max}) located between 518-532 nm (**FL-BTD**), 486-491 nm (**DBF-BTD**), 495-498 nm (**MeO-BTD**), and 527-534 nm (**BuO-BTD**). As expected, the emission wavelengths are strongly influenced by the electron-donor nature of the different substituents following a similar trend than the absorption.

The relative fluorescence quantum yields (Φ_f) were determined using quinine sulfate as a reference. In general, the Φ_f values of the derivatives in solution decrease as the polarity of the solvent increases. The highest values were found in toluene solutions, 0.91 **(DBF-BTD)**, 0.77 **(MeO-BTD)**, 0.60 **(FL-BTD)** and 0.57 **(BuO-BTD)**. Contrarily, the lowest values found were in DMSO solutions, 0.60 **(DBF-BTD)**, 0.36 **(BuO-BTD)**, 0.27 **(FL-BTD)** and 0.05 **(MeO-BTD)**. The results agree with expectations, since usually the fluorescence of this type of fluorophores is quenched in polar solvents.

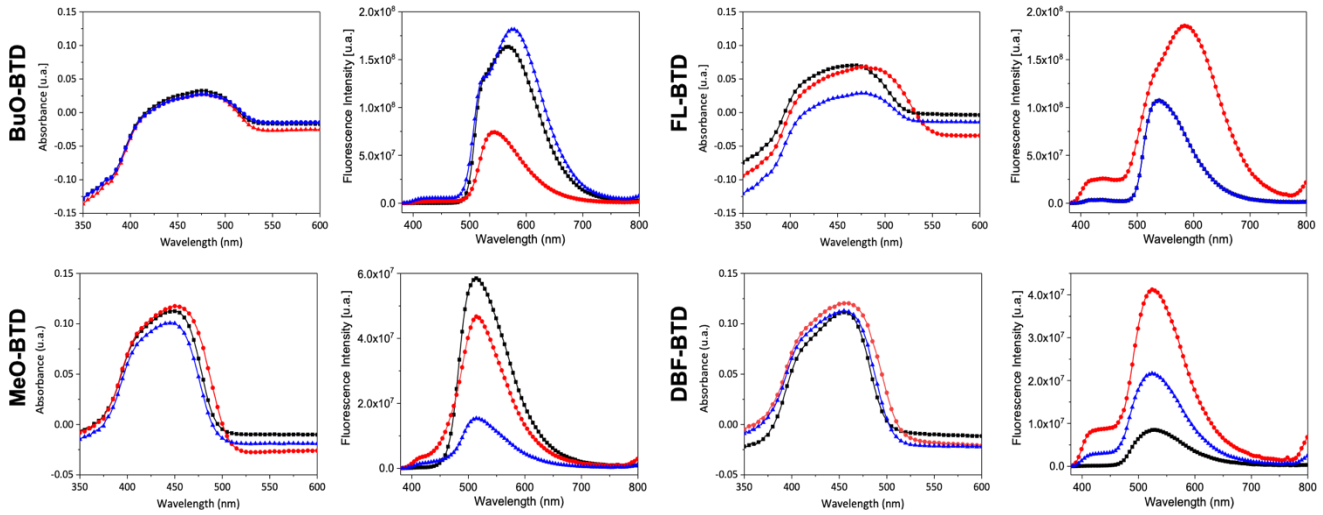

Figure 4. Solid-state absorption and emission spectra of BTD-based building blocks powders. Crystallized (black line), ground (red line) and annealed (blue line) powders.

The absorption spectra of crystallized, ground, and annealed powders display red-shifted absorption wavelengths in contrast with the absorption spectra of diluted solutions. λ_{max} is located around 469 nm (**FL-BTD**), 478 nm (**BuO-BTD**), 448 nm (**DBF-BTD**), and 455 nm (**MeO-BTD**) (figure 3). The ground powders are slightly different as compared with the crystallized and annealed powders. The red-shifting can be attributed to the π-stacking interactions established between the BTD derivatives.

The solid-state emission spectra of crystallized, ground, and annealed powders are illustrated in Figure 4. In general, strong intermolecular interactions, such as π-stacking, in combination with densely-pack arrangements led to emission quenching. The well-known fluorescence displayed by alkoxy-substituted benzothiadiazoles[24,25] such as **BuO-BTD** is still present in the fluorene-substituted derivative. We expect that the inclusion of the extended aromatic moiety will favor the formation of aggregates of π-stacked units in the solid state while retaining the emissive behavior in solution. For all compounds, the emission maxima (λ_{max}), located at 540 nm (**FL-BTD**), 546 nm (**BuO-BTD**), 532 nm (**DFB-BTD**), and 516 nm (**MeO-BTD**) are red-shifted when compared to the fluorescence in solution. Nevertheless, the Stokes shifts were less pronounced than in solution, between 61 and 86 nm, the fluorene and butoxy derivatives displaying the largest values (Table 1).

Electronic properties and quantum chemical computations

The capacity of BTD-based derivatives to self-assemble into π-stacked layered supramolecular arrangements can be exploited to fine-tune the optical properties of these compounds, as described above. An initial assessment to determine the potential application of the BTD-based building blocks (**FL-BTD**, **BuO-BTD**, **DBF-BTD** and **MeO-BTD**) as organic semiconductors was based on the exploration of how the different D-A-D architectures modify the electronic properties (frontier orbital energies and redox) by means of cyclic voltammetry (CV) and quantum chemical computations.

Density functional Theory (DFT) and Time-Dependent Density functional Theory (TD-DFT) calculations were performed to estimate the energy of the frontier molecular orbitals and to characterize the most relevant electronic transitions of the BTD-based building blocks. The selected computational protocol provides remarkable agreement with the observed solvent-dependent response in both UV-Vis absorption and fluorescence (*see Quantum Chemical Calculations* section and *ESI*).

To visualize the electronic excitations in terms of electron-hole pairs, the natural transition orbitals of the BTD-based building blocks are depicted in Figure 5.[37] In all cases; the electron is promoted from the flanking donor moieties towards the central BTD unit, in a charge-transfer from the electron-donating portion to the benzothiadiazole acceptor unit of the molecules. In all cases, only small remnants of electron density in the phenylene bridge are present. According with the theoretical results, the molecular π→π* orbitals correspond to the HOMO and LUMO respectively. All the derivatives exhibited a maximum absorption band corresponding to H→L. Relevant data for computing energy levels of the frontier

orbitals in conjunction with the energy gap are summarized in tables S3-S7.

The gaps of frontier orbital energies, HOMO-LUMO (EgOpt), of benzothiadiazole derivatives were extracted from the absorption spectra in solution, ranging from 2.86-2.94 eV (**FL-BTD**), 2.87-2.93 eV (**BuO-BTD**), 3.08-3.20 eV (**DBF-BTD**) and 3.13-3.24 eV (**MeO-BTD**). The calculated gaps (EgCalcd) were consistent with the experimental results; ranging from 2.95-2.98 eV (**FL-BTD**), 2.98-3.04 eV (**BuO-BTD**), 3.08-3.29 eV (**DBF-BTD**) and 3.23-3.313 eV (**MeO-BTD**). Analyzing the solvation effect on the energy gap, the lower values correspond to the experiments carried out in toluene, a non-polar aromatic solvent, while the larger values are correlated with the experiments carried out in polar solvents. We can attribute this behavior to strong solute and non-polar aromatic solvent intermolecular interactions, resulting in the stabilization of the molecule and a reduction of the HOMO-LUMO energy gap. It should be noted that the BTD derivatives with oxygen and alkyl chains also have a low energy band gap when they are dissolved in aprotic polar solvents, probably due stabilizing dipole-dipole interactions.

In addition, the electrochemical properties of BTD-based building blocks were determined by cyclic voltammetry (Figure 6). Each compound can be easily reduced to a stable radical anion due to the strong accepting behavior of the benzothiadiazole moiety, and reduction is reversible in all scenarios. Further, the formal reduction potential of this event (defined as the average of the peak cathodic and anodic potentials) is virtually insensitive to the identity of flanking donors, highlighting the chemical stability of the BTD subunit radical anion. The electrochemical behavior of the donor groups, in contrast, differs for each molecule. In **BuO-BTD**, two discrete and reversible oxidation steps are discernible; these can be unambiguously ascribed to stepwise electron removal from each flanking group. The system **FL-BTD** affords an electroactive, yet dissimilar product as evinced by the starkly different profile observed during cathodic and anodic sweeps. The identity of the corresponding product remains admittedly unclear. Finally, both **MeO-BTD** and **DBF-BTD** display irreversible, fast two-electrons oxidation, yielding non-electroactive products as seen in the lack of a reduction peak during reverse scanning.

HOMO energy was determined using the oxidation potential that is related to the ionization potential (IP), because it implies the minimum energy necessary to remove an electron from the system. Likewise, we determined the LUMO energy using the reduction potential, which is related to electronic affinity (EA) due that it implies the energy gained by dropping an electron from the vacuum level to the lowest unoccupied molecular orbital.[38-39]

The oxidation and reduction potentials were obtained by using as a reference ferrocene in dichloromethane (DCM). The value

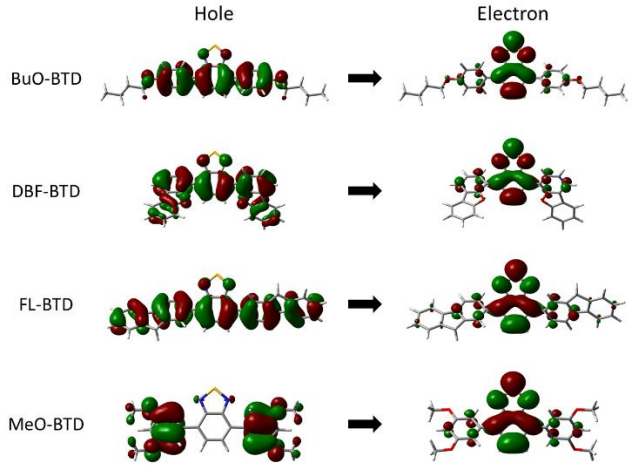

Figure 5. Natural transition orbitals for the most relevant excitation of all featured BTD-based building blocks. Calculated at the B3LYP/6-311+G(d,p) level.

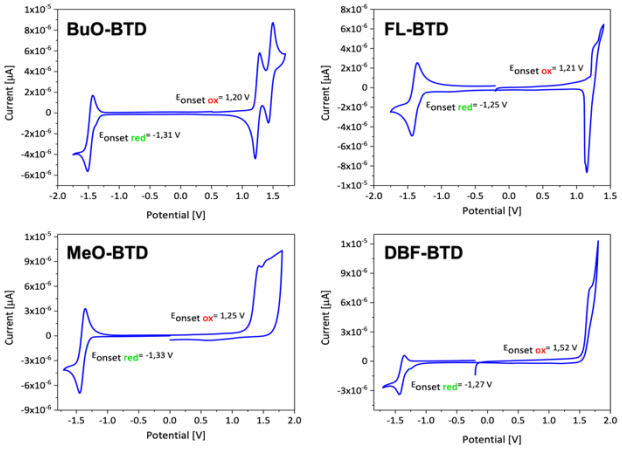

Figure 6. Cyclic voltammograms of BTD-based building blocks.

for ferrocene (Fc) with respect to the vacuum level is estimated at -4.8 eV, determined from -4.6 eV for the standard electrode potential E° of a normal hydrogen electrode (NHE) on the zero-vacuum level, and 0.2 V for Fc versus NHE.[40] The values for the HOMO and LUMO levels were obtained through equations (1) and (2) as follows:

(1) IP = HOMO = - ($E_{ox(onset)}$ + 4.8) eV
(2) EA = LUMO = - ($E_{red(onset)}$ + 4.8) eV

	$E_{ox\ (onset)}$ (V)	$E_{red\ (onset)}$ (V)	HOMO[a] (eV)	LUMO[a] (eV)	EgEc[b] (eV)
FL-BTD	1.21	-1.25	-6.01	-3.55	2.46
BuO-BTD	1.20	-1.31	-6.00	-3.49	2.51
DBF-BTD	1.52	-1.27	-6.32	-3.53	2.79
MeO-BTD	1.25	-1.33	-6.05	-3.47	2.58

Table 2. The HOMO/LUMO energy values and electrochemical energy gap. [a] Calculated from Eox (onset) and Ered (onset). [b] Calculated by the difference between the HOMO and LUMO.

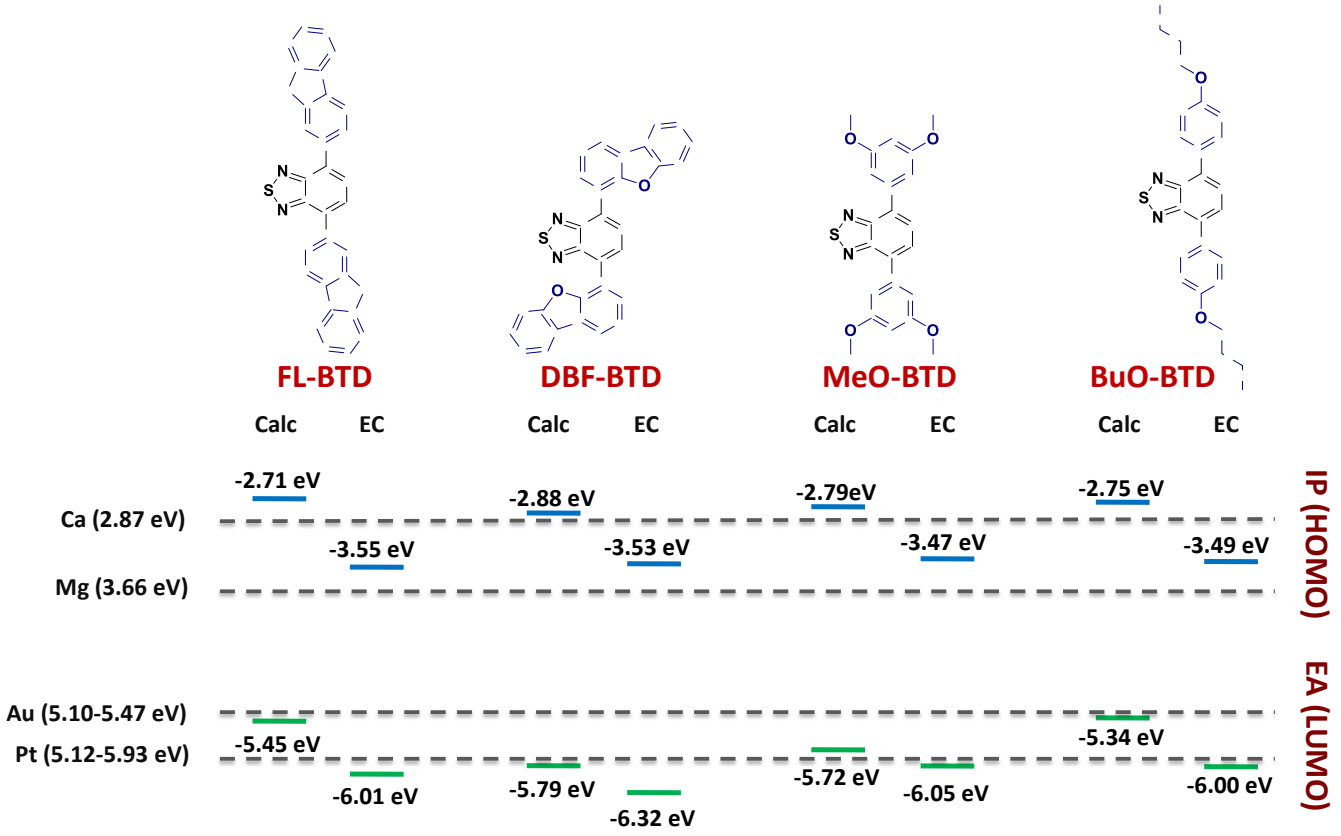

Figure 7. Experimental and calculated IP and EP values of BTD-based building blocks.

The EA was calculated as the finite difference between neutral and anion energies, and the IP was obtained as the finite difference between cation and neutral energies.[41] The calculated IP/EA energies were: 5.45/2.71 eV (**FL-BTD**), 5.34/2.75 eV (**BuO-BTD**), 5.79/2.88 eV (**DBF-BTD**) and 5.72/2.79 eV (**MeO-BTD**). The HOMO/LUMO energy values obtained were: -6.01/-3.55 (**FL-BTD**), -6.00/-3,49 eV (**BuO-BTD**), -6.32/-3.53 (**DBF-BTD**) and -6.05/-3.47 (**MeO-BTD**). Derived from these results, the electrochemical energy gap (EgEc) values are 2.46 (**FL-BTD**), 2.51 (**BuO-BTD**), 2.79 for (**DBF-BTD**) and 2.58 for (**MeO-BTD**).

The calculated and experimental IP and EA energies values are comparable to the typical semiconductors of interest in organic electronics. Threshold values of IP > 5.7 eV and EA > 3 eV have been proposed as markers of potentially efficient electron-transporting layers for n-type semiconductors.[42-43] Compounds **DBF-BTD** and **MeO-BTD** appear as the closest candidates to these suggested values, yet their propensity to irreversible oxidation may lead to their decomposition. In this sense, despite its relatively low IP, **BuO-BTD** is stable upon one- and two-electron oxidation, while showcasing an EA value close to 3 eV. Hence, this compound emerges as a promising candidate, which is also prone to facile crystallization with extensive π-stacking.

IP and EA are relevant to the hole and electron transport in a semiconductor material because in the solid-state the electrons located in the valence band (associated with the IP) can be promoted to the conduction band (associated with the EA), resulting in the formation of an electron-hole of charge carriers, which can be collected by metallic electrodes.[44] Hence, it is important that the work function of metals and IP and EA energies converge. In this context, figure 7 shows the IP (HOMO) and EA (LUMO) energies obtained from the electrochemical (EC) and theoretical (Calcd) methods, and the work function of metals used as electrodes in optoelectronic devices.[45] Taking into account that HOMO represents the donor character, if the BTD derivatives had a donor character, they can work with a gold or platinum electrode; because the electrode can accept an electron from the proximal molecule, forming a hole that will be spread throughout the material. On the contrary, if the BTD derivatives had an acceptor character, they can work with calcium or magnesium electrodes; because BTD can accept and electron from the electrode, creating a charge that will be spread throughout the material. In both cases a flow of charge carriers would be created through the material.

Finally, we determined the optical band gap between the valence band (VB) and conduction band (CB) by means of solid-state absorption using an integrating sphere and Tauc's plots (see ESI).[46] The solid samples exhibit a decrease in the

energy gap for all BTD derivatives (table 3). These results are expected due to the intermolecular interactions present in the solid-state.

	E_g^{Calcd} HOMO/LUMO	$^aE_g^{Opt}$ HOMO/LUMO	E_g^{Ec} HOMO/LUMO	$^bE_g^{Opt}$ HOMO/LUMO
FL-BTD	2.97	2.46	2.88	2.43
DBF-BTD	3.25	2.79	3.12	2.57
MeO-BTD	3.26	2.58	3.23	2.54
BuO-BTD	2.99	2.51	2.89	2.43

Table 3. Calculated, [a]optical (DCM solution), electrochemical, and [b]optical (solid) band gap energies (Eg).

Experimental

Materials and methods

Starting materials were purchased from commercial suppliers and used without further purification. Solvents were dried by standard methods or distilled prior to use. Solvents HPLC and spectroscopic grade were used for absorption, emission and recrystallization. Reactions were monitored by thin-layer chromatography (TLC) on pre-coated silica gel plates (ALUGRAM SIL G/UV_{254}) revealed by exposure to a UV_{254} lamp. ^1H and ^{13}C NMR experiments were recorded with a JEOL 400 MHz equipment using deuterated chloroform as solvent. Chemical shifts (δ) are reported in ppm and coupling constants are reported in Hz. Melting points were measured in an Electrothermal Mel-Temp® apparatus and are uncorrected. Infrared spectra were recorded on a Perkin Elmer Spectrum 400 spectrometer as solid samples using Attenuated Total Reflectance (ATR). The signals are reported in wavenumber ν (cm^{-1}). High resolution mass spectrometry (HRMS) data were acquired in an Agilent Technologies ESI-TOF spectrometer.

UV-Vis absorption and emission spectroscopy

Absorption studies were performed on a UV/VIS Lambda 35 Perkin Elmer spectrophotometer. Measurements were recorded in a wavelength region of 300–800 nm and carried out in 1 cm path length quartz cells at room temperature in different solvent solutions (HPLC grade). The UV-Vis spectra profiles in solid-state were determined on a Perkin-Elmer Lambda 950 spectrophotometer with integrating sphere in a wavelength region of 400–600 nm at room temperature. Fluorescence emission spectra were acquired on a LS55 Perkin Elmer fluorescence spectrometer; the wavelength of maximum absorption was employed as the excitation radiation.

The measurements of relative fluorescence quantum yield were carried out using quinine sulfate in 0.1 M H_2SO_4 solution (literature quantum yield is 0.54)[47] as the reference. The quantum yield was calculated according to the following equation:

$$QY_x = QY_S \times (m_x/m_s) \times (n_x/n_s)^2$$

Where the subscript *S* represents standard, quinine sulfate, and *X* represents the sample, *n* refers to the refractive index for each solvent, *m* is the slope of the curve from the plot of the integrating fluorescence intensity against absorbance.

Quantum chemical calculations

The modelling of light absorption and emission in the studied molecules was performed using density functional theory (DFT) as implemented in Gaussian 16.[48] The hybrid functional B3LYP was used throughout the study,[49] with the augmented triple-zeta polarized basis set 6-311+g(d,p).[50-51] Solvation was modelled using the implicit conductor-like polarizable continuum (CPCM) model with the dielectric constant of $CHCl_3$, PhMe and DMSO. All optimized geometries in the ground and excited states were confirmed as minima in their corresponding potential energy surface by the absence of imaginary eigenvalues upon hessian diagonalization. Excited-state geometries were optimized with the same functional and basis set, using the time-dependent DFT formalism, targeting the first root in all cases. Electron affinity and ionization potential were estimated by computing the total electronic energies of neutral, cationic and anionic molecules of the completely optimized molecular structures.

Powder X-ray diffraction experiments

PXRD experiments were carried out using a PANalytical MPD X'PertPRO diffractometer [Cu-$K_{\alpha 1}$ radiation, Ge (111) monochromator, X'Celerator detector] within the 2θ range 5-90° at a scan speed of 30° per hour. The solids were subjected to thermal and mechanical treatments. The thermal treatment was carried out in a LINKAM temperature control system from 25 degrees to 100 degrees with a speed of 0.5 degrees per minute. The mechanical treatment was carried out by grinding samples during 20 min.

Thermal analysis

The thermal characterization of the BTD derivatives was carried out using a simultaneous thermal analyzer NETZSCH model STA409PC. The sample was placed in the analyzer an aluminum sample pan under nitrogen atmosphere. To obtain the thermogram, the weight loss of the sample and the temperature were recorded in four second intervals, in a temperature range of 25 to 800 ºC with a temperature ramp of 5ºC / min, in a nitrogen atmosphere and with a quantity sample of 5 to 10 mg. NETZSCH proprietary software was used to calculate the rate of weight loss versus temperature, in this way the DSC curve was obtained.

Cyclic voltammetry

Cyclic voltammetry (CV) experiments were carried out with a potentiostat Autolab PGSTAT100 at room temperature in a homemade airtight three-electrode cell connected to a vacuum/argon line. The reference electrode consisted of a saturated calomel electrode (SCE) separated from the solution by a bridge compartment. The counter electrode was a platinum wire of approximately 1 cm^2 apparent surface. The working electrode was glassy carbon (GC) microdisk (1.0 mm of diameter–Biologic SAS). The supporting electrolyte (nBu_4N)[PF_6] (Fluka, 99% puriss electrochemical grade) and the solvent CH_2Cl_2 were used as received and simply degassed under argon. The solutions used during the electrochemical studies were typically 10^{-3} M in compound and 0.1 M in supporting electrolyte. Before each measurement, the solutions were degassed by bubbling argon and the working electrode was polished with a polishing machine (Presi P230). Potentials are given versus the Fc^+/Fc couple as internal standard ($E_{1/2}$ = 0.4 V/SCE).

Synthetic procedures

General procedure for the synthesis of BTD-based derivatives

In a dry, round-bottom flask, previously degassed 4,7-dibromobenzo[c]-1,2,3-thiadiazole (0.29 g, 1 mmol), boronic acid (2.20 mmol) and $Pd(PPh_3)_4$ (0.10 g, 10% mmol) were added. Afterwards, toluene (25 mL) and K_2CO_3 (4 mmol, 0.55 g in 2.5 mL of water) were added dropwise under argon atmosphere. The reaction mixture was refluxed until total starting materials consumption (16 to 24 h). Then, the reaction mixture was cooled to room temperature and evaporated to dryness. The resulting solid was dissolved in $CHCl_3$ (150 mL), washed with saturated NH_4Cl (2 x 100 mL), brine solution (2 x 100 mL) and distilled water (1 x 100 mL), dried over Na_2SO_4 anhydrous and evaporated to dryness. The crude products were purified by successive recrystallizations with CH_3Cl/toluene mixtures.

4,7-bis(4'-butoxyphenyl)benzo[c][1,2,3]thiadiazole (BuO-BTD)

Yellow crystalline solid (82 % yield). Melting point (°C): 128.4–129.3. FTIR-ATR (ν, cm^{-1}): 2957, 2927, 1605, 1517, 1465, 1252, 1177, 971, 826, 524. ^{1}H-NMR [400 MHz, $CDCl_3$] (δ, ppm): 7.91 (d, *J* = 8.9 Hz, 2H, H-2', H-6'), 7.71 (s, 1H, H-5, H-6), 7.07 (d, *J* = 8.9 Hz, 2H, H-3', H-5'), 4.06 (t, *J* = 6.5 Hz, 2H, H-8'), 1.82 (q, *J* = 6.5 Hz, 2H, H-9'), 1.53 (h, *J* = 7.4 Hz, 2H, H-10'), 1.01 (t, *J* = 7.4 Hz, 3H, H-11'). ^{13}C-NMR [100 MHz, $CDCl_3$] (δ, ppm): 159.35 (C-4'), 154.21 (C-4a, C-7a), 132.33 (C-1'), 130.44 (C-2', C-6'), 129.77 (C-5, C-6), 127.25 (C-4, C-7), 114.64 (C-3', C-5'), 67.80 (C-8'), 31.34 (C-9'), 19.29 (C-10'), 13.89 (C-11'). HRMS (ESI-TOF): calculated for $C_{26}H_{29}N_2O_2S$, 433.19497. Found for 433.19499 [$M^+ + H^+$] (error: 0.03 ppm).

4,7-di(9H-fluoren-2-yl)benzo[c][1,2,3]thiadiazole (FL-BTD)

Yellow crystalline solid (85 % yield). Melting point (°C): 290.6–291.6. FTIR-ATR (ν, cm^{-1}): 3038, 2009, 1955, 1606, 1546, 1452, 1395, 824, 738, 517. ^{1}H-NMR [400 MHz, $CDCl_3$] (δ, ppm): 8.20 (s, 1H, H-5, H-6), 8.02 (d, *J* = 7.9 Hz, 1H, H-4'), 7.97 (d, *J* = 8.1 Hz, 1H, H-5'), 7.92 (s, 1H, H-1'), 7.92-7.85 (d, *J* = 7.5 Hz, 1H, H-3'), 7.62-7.60 (d, *J* =7.0 Hz, 1H, H-8'), 7.47-7.39 (t, 1H, H-6'), 7.39-7.31 (t, 1H, H-7'), 4.10 (s, 2H, H-9'). ^{13}C-NMR [100 MHz, $CDCl_3$] (δ, ppm): 143.69 (C-4a, C-7a), 143.62 (C-2'), 142.30 (C-8b'), 141.14 (C-8a'), 139.97 (C-8'), 135.98 (C-4b'), 135.30 (C-4a'), 133.54 (C-1'), 128.10 (C-4'), 126.99 (C-4, C-7), 126.87 (C-5, C-6), 125.90 (C-7'), 125.10 (C-6'), 120.16 (C-3'), 120.00 (C-5'), 37.10 (C-9'). HRMS (ESI-TOF): calculated for $C_{32}H_{21}N_2S$, 465.14254. Found for 465.14210 [$M^+ + H^+$] (error: 0.94 ppm).

4,7-bis(dibenzo[b,d]furan-4-yl)benzo[c][1,2,3]thiadiazole (DBF-BTD)

Yellow crystalline solid (65 % yield). Melting point (°C): 306.1 – 307.0. FTIR-ATR (ν, cm^{-1}): 3039, 1587, 1577, 1452, 1262, 1187, 897, 835, 738, 515. ^{1}H-NMR [400 MHz, $CDCl_3$] (δ, ppm): 8.36 (s, 1H, H-5, H-6), 8.16 (d, *J* = 8.8 Hz, 1H, H-1'), 8.07 (dd, *J* = 11.0, 6.7 Hz, 2H, H-3', H-9'), 7.58 (t, *J* = 7.7 Hz, 2H, H-2', H-6'), 7.49 (t, J = 7.7 Hz, 1H, H-7'), 7.41 (t, J = 7.6 Hz, 1H, H-8'). ^{13}C-NMR [100 MHz, $CDCl_3$] (δ, ppm): 188.36 (C-4a, C-7a), 183.72 (C-4a'), 178.24 (C-4b'), 141.43 (C-4, C-7), 139.97 (C-5, C-6), 135.55 (C-4'), 130.20 (C-7'), 130.20 (C-3'), 128.67 (C-9a'), 127.35 (C-2'), 126.46 (C-9b'), 122.95 (C-9'), 120.79 (C-8'), 111.84 (C-1'), 106.40 (C-6'). HRMS (ESI-TOF): calculated for $C_{30}H_{17}N_2O_2S$, 469.10107. Found for 469.10086 [$M^+ + H^+$] (error: 0.46 ppm).

4,7-bis(3',5'-dimethoxyphenyl)benzo[c][1,2,3]thiadiazole (MeO-BTD)

Yellow crystalline solid (77 % yield). Melting point (°C): 132.5–133.4. FTIR-ATR (ν, cm^{-1}): 2999, 2934, 2837, 1597, 1357, 1207, 1154, 1062, 930, 822, 689, 575. ^{1}H-NMR [400 MHz, $CDCl_3$] (δ, ppm): 7.78 (s, 1H, H-5, H-6), 7.12 (s, 2H, H-2', H-6'), 6.58 (s, 1H, H-4'), 3.89 (s, 6H, H-8', H-10'). ^{13}C-NMR [100 MHz, $CDCl_3$] (δ, ppm): 160.84 (C-3', C-5'), 153.97 (C-4a, C-7a), 139.23 (C-1'), 133.40 (C-4, C-7), 127.99 (C-5, C-6), 107.60 (C-2', C-6'), 100.40 (C-4'), 55.49 (C-8', C-10'). HRMS (ESI-TOF): calculated for $C_{22}H_{21}N_2O_4S$, 409.12220. Found for 409.12270 [$M^+ + H^+$] (error: 1.22 ppm).

Conclusions

Benzothiadiazole-based D-A-D derivatives can be readily accessed through Pd-catalyzed coupling reactions in moderate to good yields. The featured compounds combine ionization potentials and electron affinities close to those recommended for n-type semiconductors, while displaying reversible reduction events in all cases due to the electronegative and stable BTD heterocycle. The solid-state ordering of the compounds is crystalline, as inferred from PXRD experiments, with minor response to thermal or mechanical stimuli. This is desirable for their incorporation into organoelectronic devices, as it suggests that the compounds retain their supramolecular structure despite external stress.

Additionally, in an integral manner, the results indicate that the BTD derivatives analyzed in this work have potential to be used as semiconductor materials, not only because of their electronic properties, but also because the compounds can be obtained through a simple one-step synthesis, the isolation of the derivatives is highly processable and they are obtained with a high degree of purity; which implies that obtaining these compounds can be easily scalable. On the other hand, it should be noted that the analyzed compounds shown high stability as revealed by the thermal analysis; a property desired in semiconductor materials.

Author Contributions

Montserrat Miranda-Olvera, Rafael Arcos-Ramos: Conceptualization, Investigation, Methodology, Characterization, Formal analysis, Writing original draft. ***Mauricio Maldonado-Domínguez:*** Modelling, Data analysis, Writing original draft. ***Lionel Salmon, Gábor Molnár:*** Validation, Supervision, Resources, Writing original draft. ***María del Pilar Carreón-Castro, Azzedine Bousseksou:*** Funding acquisition, Project administration, Supervision.

Conflicts of interest

There are no conflicts to declare.

Acknowledgements

MDP Carreón-Castro acknowledges to DGAPA-UNAM (PAPIIT IN-207421) and to SEP-CONACYT-ANUIES-ECOS Francia (296682) Ingeniería de películas delgadas basadas en compuestos de transición de espín para aplicaciones en micro(opto)electromecánicos. RMMO would like to thank to CONACYT for the granted scholarship (Grant number 335895). The work has been performed within the framework of the French-Mexican International Laboratory (LIA-LCMMC). This work was supported by the Ministry of Education, Youth and Sports of the Czech Republic through the e-INFRA CZ (ID:90140).

Notes and references

1 F. Silvestri, A. Marrocchini, M. Seri, C. Kim, T.J. Marks, A. Facchetti, A. Taticchi, *J. Am. Chem. Soc.*, 2010, **132**, 6108-6123.
2 J. Mei, Y. Diao, A.L. Appleton, L. Fang, Z. Bao, *J. Am. Chem. Soc.*, 2013, **135**, 6724-6746.
3 W. Jiang, Y. Li, Z. Wang. *Chem. Soc. Rev.*, 2013, **42**, 6113-6127.
4 H. Sirringhaus, *Adv. Mater.*, 2014, **26**, 1319-1335.
5 H. Lin, S. Chen, Z. Li, J.Y.L. Lai, G. Yang, T. McAfee, K. Jiang, Y. Li, Y. Liu, H. Hu, J. Zhao, W. Ma, H. Ade, H. Yan, *Adv. Mater.*, 2015, **27**, 7299-7304.
6 B. Kan, M. Li, Q. Zhang, F. Liu, Z. Wang, Y. Wang, W. Ni, F. Long, X. Yang, H. Feng, Y. Zuo, M. Zhang, F. Huang, Y. Cao, T.P. Russell, Y. Chen, *J. Am. Chem. Soc.*, 2015, **137**, 3886-3893.
7 W. Ma, G. Yang, K. Jiang, J.H. Carpenter, Y. Wu, X. Meng, T. McAfee, J. Zhao, C. Zhu, C. Wang, *Adv. Energy. Mater.*, 2015, **5**, 1501400.
8 Y. Liu, J. Zhao, Z. Li, C. Mu, W. Ma, H. Hu, K. Jiang, G. Lin, H. Ade, H. Yan, *Nat. Commun.,* 2014, **5**, 5293.
9 L. Duan, J. Quiao, Y. Sun, Y. Qiu Y, *Adv. Mater.*, 2011, **23**, 1137-1144.
10 X. Zhang, Z. Ma, Y. Yang, X. Zhang, X. Jia, Y. Wei, *J. Mater. Chem. C*, 2014, **2**, 8932-8939.
11 J.N. Clifford, E. Martínez-Ferrero, A. Viterisi, E. Palomares, *Chem. Soc. Rev.*, 2011, **40**, 1635-1646.
12 M. Velusamy, K.R. Justin Thomas, J.T. Lin, Y.C. Hsu, K.C. Ho, *Org. Lett.*, 2005, **7**, 1899-1902.
13 W. Zhu, Y. Wu, S. Wang, W. Li, X. Li, J. Chen, Z.S. Wang, H. Tian, *Adv. Funct. Mater.*, 2011, **21**, 756-763.
14 J. Kim, A.R. Han, J. Hong, G. Kim, J. Lee, T.J. Shin, J.H. Oh, C. Yang, *Chem. Mater.*, 2014, **26**, 4933-4942.
15 Z. Guo, A. Facchetti, T.J. Marks, *Chem. Rev.*, 2014, **114**, 8943-9021.
16 M.K. Chini, R.Y. Mahale, S. Chatterjee, *Chem. Phys. Lett.*, 2016, **661**, 107-113.
17 Y. Niu, P. Wang, L. Pu, Y. Zhang, *Dyes Pigm.*, 2019, **170**, 107594.
18 D.B. Shaikh, A.A. Said, Z. Wang, P.S. Rao, R.S. Bhosale, A.M. Mak, K. Zhao, W. Liu, W. Gao, J. Xiw, S.V. Bhosale, S.V. Bhosale, Q. Zhang, *ACS Appl. Mater. Interfaces*, 2019, **47**, 44487-44500.
19 Y.J. Cheng, Y.J. Ho, C.H. Chen, W.S. Kao, C.E. Wu, S.L. Hsu, C.S. Hsu, *Macromolecules*, 2012, **45**, 2690-2698.
20 P. Sonar, S.P. Sing, S. Sudhakar, A. Dodabalapur, A. Sellinger, *Chem. Mater.*, 2008, **20**, 3184-3190.
21 P. Sonar, S.P. Singh, P. Leclere, M. Surin, R. Lazzaroni, T.T. Lin, A. Dodabalapur, A. Sellinger, *J. Mater. Chem.*, 2009, **19**, 3228-3237.
22 N.J. Findlay, B. Breig, C. Forbes, A.R. Inigo, A.L. Kanibolotsky, P.J. Skabara, *J. Mater. Chem. C*, 2016, **4**, 3774-3780.
23 J. Du, M.C. Biewer, M.C. Stefan, *J. Mater. Chem. A*, 2016, **4**, 15771-15787.
24 X. Zhang, H. Gorohmaru, M. Kadowaki, T. Kobayashi, T. Ishi-I, T. Thiemann, S. Mataka, *J. Mater. Chem.*, 2004, **14**, 1901-1904.
25 X. Zhang, R. Yamaguchi, K. Moriyama, M. Kadowaki, M. Kobayashi, T. Ishi-I, T. Thiemann, S. Mataka, *J. Mater. Chem.*, 2006, **16**, 736-740.
26 L.D.O. Aguiar, E. Regis, P. Tuzimoto, E. Girotto, I.H. Bechtold, H. Gallardo, A.A. Vieira, *Liq. Cryst.*, 2018, **45**, 49-58.
27 J.P. Heiskanen, P. Vivo, N.M. Saari, T.I. Hukka, T. Kastinen, K. Kaunisto, H.J. Lemmetyinen, O.E.O. Hormi, *J. Org. Chem.*, 2016, **81**, 1535-1546.
28 Y. Wang, T. Michinobu, *J. Mater. Chem. C*, 2016, **4**, 6200-6214.
29 R. Martín, P. Prieto, J.R. Carrillo, A.M. Rodríguez, A. de Cozar, P.G. Boj, M.A. Díaz-García, M.G. Ramírez, *J. Mater. Chem. C*, 2019, **7**, 9996-10007.
30 H. Fang, H. Gao, T. Wang, B. Zhang, W. Zing, X. Cheng, *Dyes Pigm.*, 2017, **147**, 190-198.
31 M. Echeverri, I. Martín, A. Concellón, C. Ruiz, M. San Anselmo, E. Gutiérrez-Puebla, J.L. Serrano, B. Gómez-Lor, *ACS Omega*, 2018, **3**, 11857-11864.
32 M. Castillo-Vallés, A. Martínez-Bueno, R. Giménez, T. Sierra, M.B. Ros, *J. Mater. Chem. C*, 2019, **7**, 14454-14470.
33 H. Lino, T. Usui, J.I. Hanna, *Nat. Commun.*, 2015, **6**, 6828.
34 K. He, W. Li, H. Tian, J. Zhang, D. Yan, Y. Geng, F. Wang, *ACS Appl. Mater. Interfaces*, 2017, **9**, 35427-35436.
35 J.M. Mativetsky, M. Kastler, R.C. Savage, D. Gentilini, M. Palma, W. Pisula, K. Muellen, P. Samori, *Adv. Funct. Mater.*, 2009, **19**, 2486-2494.

36 H.N. Tsao, D. Cho, J.W. Andreasen, A. Rouhanipour, D.W. Breiby, W. Pisula, K. Muellen, *Adv. Funct. Mater.*, 2009, **21**, 209-212.
37 R. L. Martin, *J. Chem. Phys. B*, 2003, **118**, 4775-4777.S.K. Seth, I. Saha, C. Estarellas, A. Frontera, T. Kar, S. Mukhopadhyay, *Cryst. Growth Des.* 2011, **11**, 3250-3265.
38 S. Janietz, D. Bradley, M. Grell, C. Giebeiber, M. Inbasekaran, E. Woo, *Appl. Phys. Lett.*, 1998, **73**, 2453-2455.
39 J. Brédas, R. Silbey, D. Boudreaux, R. Chance, *J. Am. Chem. Soc.*, 1983, **105**, 6555-6559.
40 B. D'Andrade, S. Datta, S. Forrest, P. Djurovich, E. Polikarpov, M. Thompson, *Org. Electron.*, 2005, **6**, 11-20.
41 M. Winkler and K.N. Houk, J. Am. Chem. Soc., 2007, **129**, 1805-1815.
42 E. Louis, E. San-Fabián, M.A. Díaz-García, G. Chiappe and J.A. Vergés, *J. Phys. Chem. Lett*., 2017, **8**, 2445-2449.
43 K. Zhou, H. Dong, H. Zhang, W. Hu, *Phys. Chem. Chem. Phys.*, 2014, **16**, 224448-22457.
44 H. Michaelson, *J. Appl. Phys.*, 1977, **48**, 4729.
45 P.R. Jubu, F.K. Yam, V.M. Igba, K.P. Beh, *J. Sol. State Chem.*, 2020, **290**, 121576.
46 D.F. Eaton, Reference materials for fluorescence measurement, *Pure Appl. Chem*. **60** (1988) 1107-1114.
47 Gaussian 16, Revision C.01, Frisch, M. J.; Trucks, G. W.; Schlegel, H. B.; Scuseria, G. E.; Robb, M. A.; Cheeseman, J. R.; Scalmani, G.; Barone, V.; Petersson, G. A.; Nakatsuji, H.; Li, X.; Caricato, M.; Marenich, A. V.; Bloino, J.; Janesko, B. G.; Gomperts, R.; Mennucci, B.; Hratchian, H. P.; Ortiz, J. V.; Izmaylov, A. F.; Sonnenberg, J. L.; Williams-Young, D.; Ding, F.; Lipparini, F.; Egidi, F.; Goings, J.; Peng, B.; Petrone, A.; Henderson, T.; Ranasinghe, D.; Zakrzewski, V. G.; Gao, J.; Rega, N.; Zheng, G.; Liang, W.; Hada, M.; Ehara, M.; Toyota, K.; Fukuda, R.; Hasegawa, J.; Ishida, M.; Nakajima, T.; Honda, Y.; Kitao, O.; Nakai, H.; Vreven, T.; Throssell, K.; Montgomery, J. A., Jr.; Peralta, J. E.; Ogliaro, F.; Bearpark, M. J.; Heyd, J. J.; Brothers, E. N.; Kudin, K. N.; Staroverov, V. N.; Keith, T. A.; Kobayashi, R.; Normand, J.; Raghavachari, K.; Rendell, A. P.; Burant, J. C.; Iyengar, S. S.; Tomasi, J.; Cossi, M.; Millam, J. M.; Klene, M.; Adamo, C.; Cammi, R.; Ochterski, J. W.; Martin, R. L.; Morokuma, K.; Farkas, O.; Foresman, J. B.; Fox, D. J. Gaussian, Inc., Wallingford CT, 2016.
48 A. D. Becke, *J. Chem. Phys.,* 1993, **98**, 5648-5652.
49 A. D. McLean, G. S. Chandler, *J. Chem. Phys.,* 1980, 72, 5639-5648.
50 C. Lee, W. Yang, R. G. Parr, *Phys. Rev. B*, 1988, **37**, 785-789.
51 V. Barone and M. Cossi, *J. Phys. Chem. A*, 1998, **102**, 1995-2001